The Henryk Niewodniczański
INSTITUTE OF NUCLEAR PHYSICS
Polish Academy of Sciences
152 Radzikowskiego Str., 31-342 Kraków, Poland

www.ifj.edu.pl/reports/2006.html

Kraków, October 2006

Report No. 1980/B

Innovative Mutually Inductively Coupled Radiofrequency Coils for Magnetic Resonance Imaging and Spectroscopy

Bogusław Tomanek

Habilitation Thesis

Institute for Biodiagnostics,Winnipeg and Calgary, Canada

CONTENT

GLOSSARY OF TERMS

SNR	Signal to noise ratio
B_1	Magnitude of the RF field
M_0	Magnetization
μ_0	Permeability of free space
Q	Quality factor of the coil
K	Numerical factor depending on the coil geometry
N	Filling factor
ω_0	Larmor frequency
V_c	Volume of the coil
F	Noise figure of the preamplifier
k	Boltzman Constant
T_c	Probe temperature
Δf	Bandwidth (in Hertz) of the receiver

INTRODUCTION

Magnetic Resonance Imaging (MRI) has been found to be one of the most useful diagnostic imaging techniques. Thousands of MRI systems have been produced and installed every year in clinics since its discovery about 20 years ago. MRI allows the visualization of internal structures of a body. Clinically, it is used for early disease diagnosis, while research areas cover human and animal anatomy, physiology and pathology. The image contrast comes mostly from water molecules or/and their movement. Blood flow, blood oxygenation or specific properties of tissues, called relaxation times can also be visualized to enhance the MRI capability to image pathology In addition, variety of MRI techniques can be used to obtain desired contrast and allow focusing on specific types of tissue, making this technique superior to other imaging techniques such as Computer Tomography (CT or ultrasound. MRI is used for a diagnosis of many diseases, such as cancer, stroke, brain disorder (Alzheimer) liver failure, osteoporosis, etc. MRI is also commonly used for the assessment of the surgery of the surgery or for image guided procedures such as biopsy or laparoscopy. The combination of MR imaging with spectroscopy provides a powerful tool for clinical management of problems such as stroke, tumor monitoring and the assessment of other diseases. To produce an MR image, strong magnetic field (order of 1T) generated by, most frequently, a Superconductive magnets is needed to create net magnetization of the water protons. To spatially encode spins variable magnetic fields, generated by so-called gradients coils are applied. To excite spins and receive MR signal probes producing an RF RFfield are used. Because MRI used only magnets and RF fields, unlike in CT, MRI does not use harmful radiation.

In the recognition of the importance of the application of MRI in the medicine, Dr. Paul Lauterbur and Sir Peter Mansfield were awarded the 2003 Nobel Prize for their discoveries concerning MRI.

As the signal-to-noise ratio (SNR) and thus image resolution increases with the magnetic field strength there is a trend forward using stronger magnets. The standard clinical system is equipped with a 1.5T magnet but 3T systems also obtained an FDA approval for clinical use. While stronger magnets (above 3T) are technically feasible, their possible harmful side-effects and high costs (usually 1M$ per Tesla for each unit) are the limiting factors. There are however other methods of improving SNR such as new imaging techniques or longer acquisition time. The most efficient, inexpensive and applicable to any imaging technique method of increasing image resolution is however the improvement in the RF coil design. The RF coils generate RF field and receive NMR signal. This work presents innovative designs proposed by the author and published in years 2000-2006. The major focus of the thesis is the new method of RF coil design based on mutually inductive coupling. Examples of the possible applications of the rf coils are also presented. Some of the applications, such as intraoperative MRI (Chapter 8), are possible only with this unique design. This coil was a crucial component of the first in the world Intraoperative MRI system with a moveable magnet. This project allowed the creation of the company IMRIS, Inc., that currently sells these units worldwide. The company employs, as of July 2006, over 60 people and it is worth over $60 million. An other example is a breast rf coil, that allows high resolution breast images (100μm × 100μm) to be obtained within seconds, The coil design does not require breast compression allowing painless and comfortable yet very efficient breast screening and diagnosis as it can detect submillimeter tumors. This coil provides superior

performance in comparison to any commercially available RF coil and it was used in Sidney, Australia with Siemens 3T and in Winnipeg with 1.5T GE systems for breast cancer study.

A particular attention is paid to new types of RF coils (patented by the author) bases on multi-ring assembly. The design, analysis of their parameters and a comparison to other standard coils is provided. The rings are not only inductively matched and tuned but in addition each component of the coil (each ring) is inductively coupled with each other thus allowing to avoiding any electrical connections between coil's elements. The coils provide superior performance and enable new applications impossible due to the restrictions of standard RF coils. Theoretical calculations of the RF field produced by the coils as well as applications are presented. The method of calculations resonance frequencies of each single element and the self-resonance of the entire assembly is presented.

The work was carried out at the Institute for Biodiagnotics (IBD), Winnipeg and IBD (West), Calgary, Canada. The coils were designed at IBD and installed in Winnipeg (multi-nuclear multi-ring), Calgary (head RF coil for intraoperative MRI), Sydney Australia (breast coil). The rf coils based on these design have been used since by other labs across the world.

The submitted thesis includes an Introduction, eight chapters, references and copies of five selected papers. Chapter 1 deals with signal-to-noise (SNR) issues in MR Imaging and Spectroscopy. Chapter 2 introduces inductive coupling in the RF coils design, that is base for the innovative RF coil design. Chapter 3 considers the importance of the B_1 homogeneity and SNR. Chapter 4 introduces the concept of multi-ring coils and their theoretical analysis. This chapter explains also the theory of inductive tuning of

mutually coupled elements of the RF coil. Chapter 5 shows the experimental results of the performance of the multi-ring coils. Chapter 6 is an extension of the design of the inductively coupled multi-ring to the multi-frequency multi-ring RF coil. It describes the theory construction of multi-frequency multi-ring coil, and an example of its application to liver ^{31}P MRS and MRI at the very high field (7T). Chapter 7 describes the breast RF coil and chapter 8 – an RF probe used for MRI with a movable magnet during the brain surgery.

1. SIGNAL TO NOISE RATIO AND B1 HOMOGENEITY IN MR IMAGING AND SPECTROSCOPY.

The most important parameter in Magnetic Resonance Imaging (MRI) affecting all studies is image quality, thus the resolution that depends on signal to noise ratio (SNR). Therefore both MRI and Magnetic Resonance Spectroscopy (MRS), require maximal SNR as well as homogeneous RF field (B_1) to obtain optimized images and spectra. While MRI allows the application of post-processing methods, such as correction of image intensity to correct B_1 inhomogeneities, MRS is more demanding from this point of view leaving very little opportunity for post-processing and allowing mostly hardware improvement. In addition, due to the smaller volume of interest (VOI) and metabolite concentration, there is less signal available in MRS than in MRI thus time required to obtain good spectra is long, pushing the SNR requirements to the limits.

Unfortunately when considering RF probe construction, the requirements of high SNR and good B_1 homogeneity usually conflict. The SNR depends on many factors such as the strength of the magnetic field, geometry, resistance and quality factor (Q) of the coil, sample size, filling factor of the coil, type of reception (linear or circular), etc. The B_1 field distribution depends on the geometry of the coil, its type (transmit and receive, or transmit/receive) and the material used for the coil construction.

Therefore, a trade-off among all these factors is inevitable and there is no simple, consistent recipe for making a perfect RF coil, that fulfills all the requirements for the probe for MRS and MRI. This thesis presents a new type of RF coils that virtually meets all the requirements.

The first expression describing the NMR signal was derived by Abragam (1), who showed that the electromagnetic force (emf) induced by the nuclear magnetization in the receiving coil can be expressed as:

$$\psi_{rms} \sim K\eta M_0(\mu_0 Q\omega_0 V_c / 4FkT_c\Delta f)^{1/2} \quad [1.1]$$

where K is numerical factor that depends on the coil geometry; η is the filling factor i.e. a measure of the fraction of the RF field volume occupied by the sample; M_0 is the magnetization (proportional to the magnetic field strength); μ_0 is the permeability of free space; Q is the quality factor of the coil; ω_0 is the Larmor frequency; V_c is volume of the coil; F is the noise of the preamplifier; k is Boltzman constant; T_c is the probe temperature; Δf is the bandwidth (in Hertz) of the receiver.

The above equation explains the historical tendency to introduce stronger and stronger magnets in an effort to increase SNR. Therefore, magnets generating a magnetic field of 20T were produced for *ex-vivo* MRS, while whole body MRI systems have reached 7T, and even higher field systems are under construction.

As one can notice from [eq. 1.1] (keep in mind that $M_0 \sim \omega_0$), the SNR is proportional to the 3/2 power of the magnetic field. This is true under the assumption that other factors are independent of frequency. However, a closer analysis of the dependence of noise mechanism with frequency and other factors such as RF coil shape, preamplifier noise, and other electronic components whose performance depends on, and usually degrades with the frequency, reveals a less favourable SNR relationship. The rule of thumb is a linear relationship between the SNR and the magnetic field strength for the range of frequencies used in MRI (2,3).

2. INDUCTIVE COUPLING IN THE RF COIL TUNING AND MATCHING

Probe impedance matching (4) by inductive coupling has been known in electronics theory (5). However, *mutually* inductive coupling, wherein the probe coil is the primary and a separate matching loop is the secondary, was probably first reported in NMR in 1983 in the articles on quadrature laboratory frame detection by Hoult et al. (6,7). The obvious attribute of any mutually inductive coupling is the absence of a physical connection between conductors. The work described in the thesis expands this technique and shows how mutual coupling could be used not only for tuning and matching but for the construction of innovative RF coils based on inductively coupled elements.

The simple system, shown in Fig. 2.1, where a matching coil of inductance L_1 is coupled by variable mutual inductance M_{12} to a tuned coil of inductance L_2 and capacitance C_2. If reactance $X_2 = \omega L_2 - 1/\omega C_2$, the input impedance Z_{in} is given by (1)

$$Z_{in} = j\omega L_1 + \frac{\omega^2 M_{12}^2}{r_2 + jX_2} \quad [2.1]$$

When the probe is tuned $X_2 = wL_2 - \frac{1}{\omega c_2} = 0$, where ω is angular frequency, $(L_2C_2)^{-1/2}$ is the probe frequency ω_c, r_2 is the small ($<<\omega_c L_2$) resistance of the loop and its tuning capacitor. A typical value for Z_{in} when the probe is tuned and matched is 50 ohms.

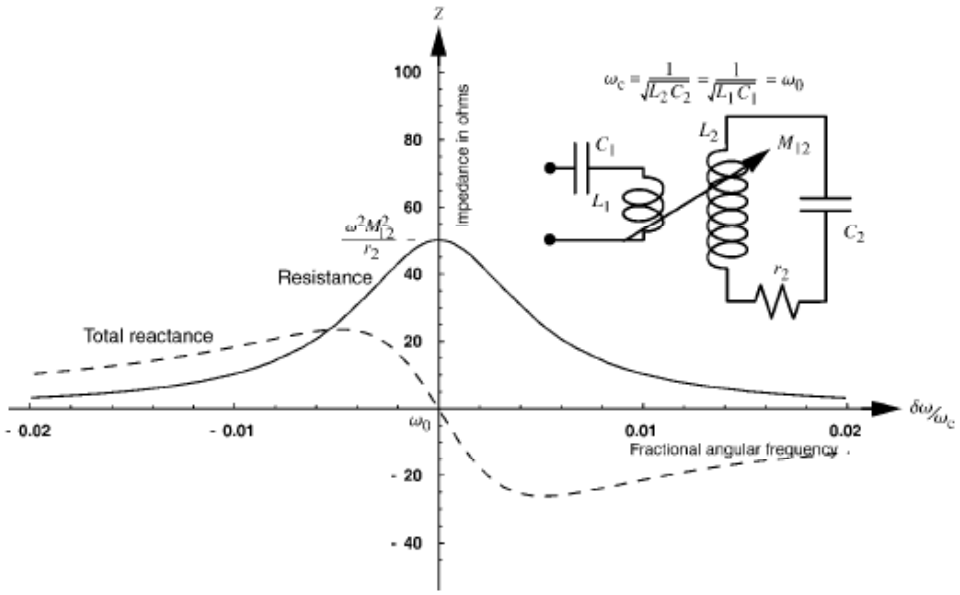

FIG. 2.1. Input impedance versus frequency of a coil coupled by mutual inductance. The matching coil is tuned to the Larmor.

At the Larmor frequency ($\omega_c = \omega_0$) when the matching coil is tuned, reactance $X_1 = \omega L_1 - 1/\omega C_1 = 0$. The input impedance is then resistive at probe resonance and, from Eq. [2.1], setting $\omega_c = \omega_0$, is given by

$$Z_{\substack{in \\ resonance}} = \frac{\omega_0^2 M_{12}^2}{r_2} \equiv \frac{Q\omega_o M_{12}^2}{L_2} \equiv Qk^2\omega_0 L_1 \qquad [2.2]$$

where Q $\left(Q = \omega L / R\right)$ is the quality factor, k $\left(k^2 = \frac{M_{12}^2}{L_1 L_2}\right)$ is the coupling constant between two loops, as shown in Fig. 2.2.

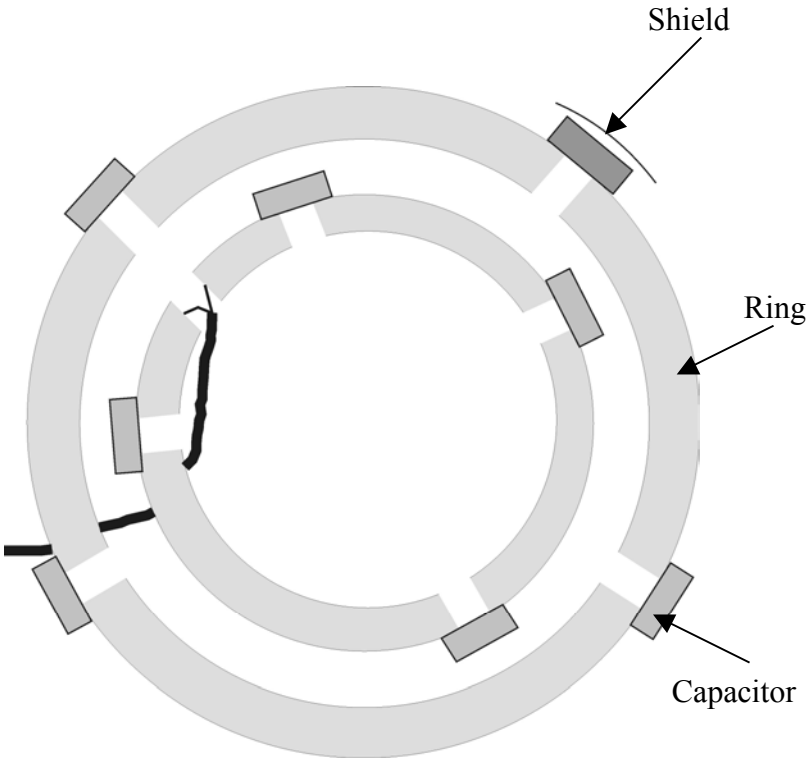

FIG. 2.2. Well-constructed surface coil with inductive matching.

The practical design of an inductively coupled surface RF coil is shown in Fig. 2.2. Both the matching ring and the tuning ring (active one) are tuned to the same frequency. The distributed, high-*Q* capacitors greatly reduce *conservative* electric fields and therefore dielectric losses in the sample. The large ring cross section helps reduce the loop inductance and therefore the strength of the electric fields while at the same time minimizing copper losses. However, as capacitance to the sample increases with a large conductor, it may be advantageous to use foil shields.

The detail analysis of the received signal and B_1 asymmetry when inductive matching is used in the presence of sample losses is described in Hoult and Tomanek (8).

3. B_1 HOMOGENEITY VS SNR IN RF COIL DESIGN

As mentioned above, B_1 homogeneity, beside SNR, is the most important parameter in MRI. Homogeneous B_1 field can be easily achieved by an application of cylindrical, such as solenoid or bird-cage, coils. However, smaller coils, so called surface coils, due to their low sensitivity and high filing factor provide much better SNR and therefore are widely used in MRI and MRS. Unfortunately, they produce inhomogeneous B_1 field. Their sensitivity decreases with increasing distance between the coil and the object of interest due to significant B_1 inhomogeneity along coil axis. Therefore images show decreasing signal intensity. If the B_1 field varies over the sample there is uncertainty of metabolites and water distribution in the MR image. Thus good B_1 homogeneity is essential. Good localized imaging is particularly important for deep internal structures such as liver, kidney, heart or some brain structures. The measurements of relaxation times in MRS also require good B_1 homogeneity or application of complex pulse sequences, like DRESS, STEAM, ISIS. (9, 10).

Various RF surface coils have been designed to optimize SNR and B_1 homogeneity from deep organ of interest in MRI. Some authors used anatomically shaped surface coils. (11) to fit the anatomical structure under examination. However SNR for such coils is lower than for traditional surface coils. In addtion image intensity varies depending on the coil shape and deep of organs being under examination.

There are two principal approaches which are used to compensate for surface coil B_1 inhomogeneity when phantom image is involved: correction matrix and digital filtering. The correction matrix method (12, 13) is based on calculation of the correction coefficients from phantom image. The correction coefficients are determined by dividing

the surface coil image into the matrix. The coefficients are then applied as a correction matrix for each image. The disadvantage of this method is that correction coefficients can be calculated only for a specific position and type of coil.

An analytic correction method was also applied to correct the signal intensity nonuniformity caused by the inhomogenous reception profile of surface coil for MRI (14, 15). In this case the Biot-Savart law was used to improve image homogeneity. Although this method does nor require any phantom experiments, the disadvantage of this method is that the theoretical model does not take into account imperfections that are present under experimental conditions. Two sets of images orthogonal to the plane of the coil are also required. Data post processing is necessary as well.

The application of separate transmitter and receiver coils is also widely used to improve B_1 homogeneity. The transmitter coil is made larger then the receiver and placed orthogonally to minimize magnetical coupling. However this method requires large transmitter power. Interaction between coils also occurs and B_1 is still relatively inhomogenious. The use of a pair of flat transmitter coils and a single flat receiver coil as a probe was also proposed (16) to minimize interaction between transmitter and receiver. Two concentric surface coils the larger working as a transmitter and the smaller as a receiver were also applied in MR spectroscopy to improve B_1 homogeneity (17 - 20). Interaction between coils was controlled by using cross diodes and a transmitter line. Such designing gives better homogeneity than single surface coil. However procedure for circuit adjustment is rather complicated. To reduce the current induced in the transmitter coil during the receive period the transmitter coil should be at least three times larger then the receiver or cross diodes in series should be added.

Another method of B_1 correction is to perform calibration experiment of a volume of interest in a large phantom (21, 22).

The thesis presents an innovative solution to generate identical fields for both excitation and receiving periods: the coil combines surface coil sensitivity with volume coil homogeneity. This idea uses two or more inductively coupled rings of different diameter, carrying current in opposite directions [Fig 3.1]. Such an assembly produces homogenous, identical excitation and receiving B_1 in the desired region of interest while providing SNR comparable with the surface coil. The coil could be used for every application.

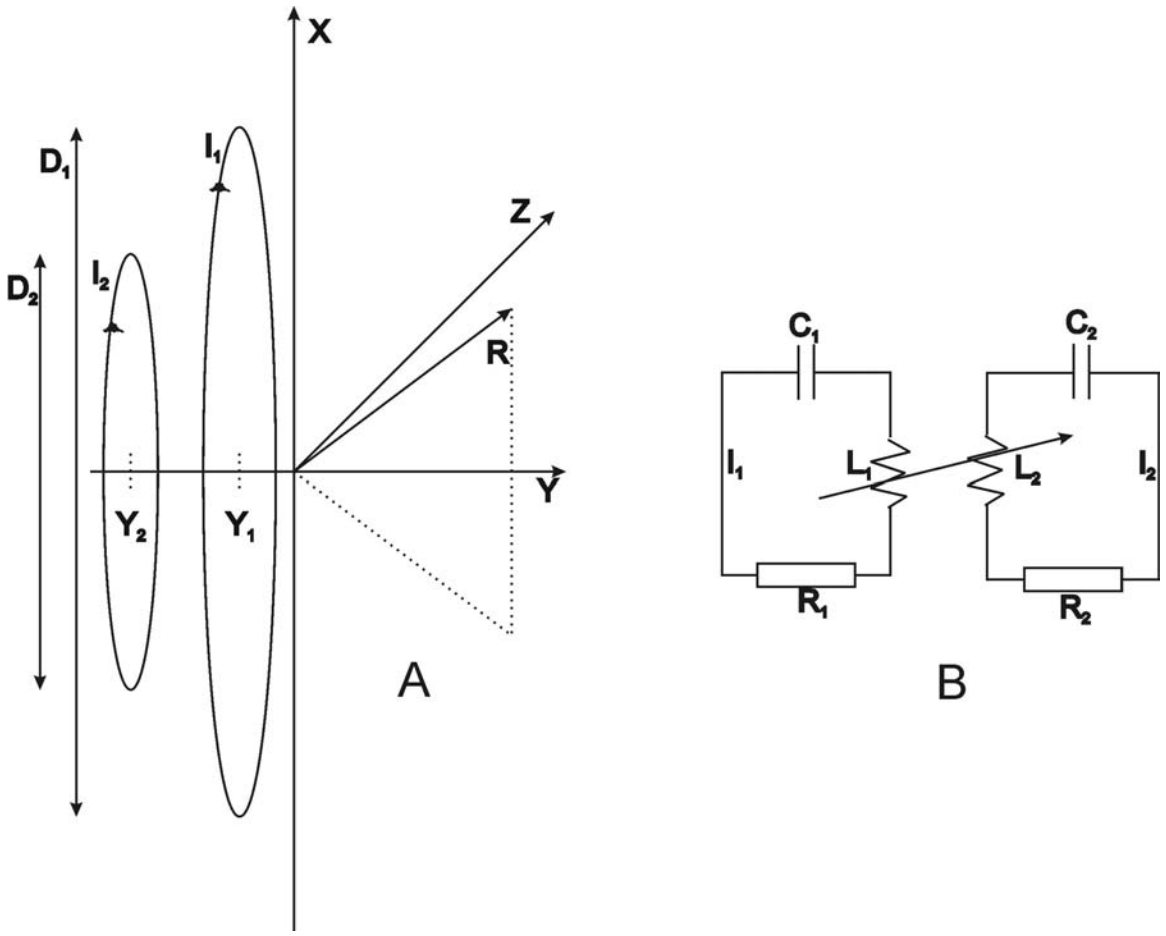

FIG. 3.1. Inductively coupled rings: Capacitors are omitted for clarity (A), Electrical schematic (B)

In this thesis the theory, application and construction of the multi-ring surface coil with very good homogeneity in specific volume of interest is described.

4. MULTI-RING COIL DESIGN AND CONSTRUCTION

The main aim of the multi-ring surface coil design is to achieve better B_1 homogeneity within the VOI, compared to standard surface coils, for improved localization, and with a minimum penalty in SNR. Design begins with optimization of the B_1 homogeneity and SNR over a specified volume. This can be accomplished with a variety of multi-ring surface coil parameters: number of rings (N), diameter (D_p), position (y_p) and current (I_p), using Bio-Savart Law Eq. [4.1]. The iteration process is then used until the optimum coil is found.

Rings are constructed from copper tubing and segmented so that the capacitance is distributed evenly to reduce conservative electric field losses within the sample. Remaining dielectric losses can be minimized with copper foil shields placed between the ring and the sample, underneath the capacitors. Non-magnetic, high-Q trimmer capacitors (Johanson, USA) are usually used for tuning the rings.

4.1 B_1 Distribution

In a static approximation, the $\mathbf{B_1}(\mathbf{r})$ field (RF field) produced by a surface coil at any point $\mathbf{r}$ in space, can be calculated from the Biot-Savart law. In the case of N separate rings, each carrying current I_p, the total field is simply a superposition of the fields from all the rings:

$$\mathrm{B}_1(\mathrm{r}) = \frac{\mu_0}{4\pi} \sum_{p=1}^{N} \oint_{l_p} \frac{I_p d\mathrm{l}_p \times (\mathrm{r} - \mathrm{r}_p)}{\left|\mathrm{r} - \mathrm{r}_p\right|^3} \qquad [4.1]$$

where μ_0 is the magnetic permeability of free space, $d\mathbf{l}_p$ is the elemental current vector of magnitude I_p, $\mathbf{r}_p$ is the position vector of the element with respect to the origin,

and the line integral is along the conductor l_p. If the coil is placed in the x-z plane, the axial B_1 field strength along the y-axis is given by:

$$B_{1y} = \frac{\mu_0}{2} \sum_{p=1}^{N} I_p \frac{a_p^2}{(a_p^2 + (y - y_p)^2)^{3/2}} \qquad [4.2]$$

where a_p is the ring radius and y_p is the position of the p^{th} ring.

4.2 Tuning Theory

The multi-ring surface coil consists of N co-axial circular rings of different diameters (D_p), currents (I_p) and axial-positions (y_p). The geometry is depicted in Fig. 3.1 (A), where an example of a two-ring coil is shown. The electrical schematic is also shown in Fig 3.1 (B). Using the theory described below, counter-rotating ring currents are possible, allowing the B_1 homogeneity to be optimized over a desired VOI.

The mutual inductance, M_{pq}, between two rings l_p and l_q is given by (23, 24)

$$M_{pq} = \frac{\mu_0}{4\pi} \oint_{l_p} \oint_{l_q} \frac{d\mathbf{l}_p \cdot d\mathbf{l}_q}{|\mathbf{r}_p - \mathbf{r}_q|}, \qquad [4.3]$$

where $\mathbf{r}_p$ and $\mathbf{r}_q$ are the position vectors of the elements $d\mathbf{l}_p$ and $d\mathbf{l}_q$ respectively. This mutual inductance can be exploited to provide the couplings necessary to distribute power appropriately from the transmitter, producing the required ring currents. For a high-Q coil, the voltage induced in any one ring is due to currents in the other N-1 rings (25). With this assumption, the voltage induced in the p^{th} ring is given by Lenz's law as $V_p = -j\omega_o \sum_{q=1, q\neq p}^{q=N} M_{pq} I_q$, where I_q is the current in the q^{th} ring. Therefore, the reactance of the p^{th} ring is given by

$$X_p = \frac{V_p}{I_p} = -j\omega_o \sum_{q=1, q\neq p}^{q=N} M_{pq} \frac{I_q}{I_p} \qquad [4.4]$$

where $\frac{I_q}{I_p}$ is the current ratio for the q^{th} and p^{th} rings, which is pre-determined by the required B_1 field. A resonant circuit tuned to the Larmor frequency has by definition, zero reactance. Therefore, to obtain the required ring-reactance (X_p) at the Larmor frequency (ω_o), it is necessary to tune each ring to a certain frequency ω_p different from ω_o.

The reactance of any ring that possesses both an inductance L_p and a capacitance C_p is given by

$$X_p = X_{L_p} + X_{C_p} = j\omega_o L_p + \frac{1}{j\omega_o C_p}. \quad [4.5]$$

The ring inductance can be approximated as $L_p \approx \mu_0 a_p \{\ln(8\frac{a_p}{b_p}) - 2\}$ (26), where a_p is the radius of the p^{th} ring and b_p is the radius of its cylindrical conductor.

The tuning capacitance required for each ring can be determined by equating the reactances in Eq. [4.4] and Eq. [4.5], such that, $\frac{1}{j\omega_0 C_p} = X_p - X_{L_p}$. The resonant frequency of each ring is then given by

$$\omega_p = \frac{1}{\sqrt{L_p C_p}}. \quad [4.6]$$

After tuning each of the N-rings to the appropriate frequency ω_p, they are brought together to form the multi-ring surface coil. The N-rings couple to create N-resonant modes each at a different frequency. In the multi-ring surface coil designs for MRI, it is the highest frequency mode that has the desired Larmor frequency (ω_0) and B_1 response.

5. MULTI-RING COIL PERFORMANCE

A series of experiments were carried out to test the performance of the multi-ring RF coil designed for the 3T system (127.77 MHz). For a comparison to the multi-ring surface coil, a 5.0 cm diameter standard surface coil (matching ring 3.2 cm in diameter) was chosen. For comparisons to a volume coil, a circularly-polarized (CP), 16 element, high-pass birdcage head coil (30 cm long, 26 cm diameter) (Morris Instruments Inc., Canada) was used.

For all simulations, the STEAM sequence was applied to select a 1 cm^3 voxel at a depth of 2.0 cm below the surface of a phantom. A 0.5 cm gap was assumed between the coil and the phantom surface so that the distance from the center of a circular surface coil to the voxel is $d = 2.5$ cm.

Experimental SNR measurements were obtained from a small hollow $1.4 \times 1.4 \times 1.4$ cm^3 cube filled with 100% mineral oil and fixed at a depth of 2.0 cm from the surface of the same 4.5L phantom filled only with 0.3% NaCl. A 1.0 cm^3 voxel was chosen within the small cube (to reduce the possibility of outer voxel contamination) and unsuppressed spectra were taken. For SNR measurement of the head coil, the voxel was chosen at the center of the phantom. SNR was evaluated from the height of the mineral oil peak. The amount of contamination due to signal originating from outside the VOI was found from the amount of water signal present in these mineral oil spectra.

Coil	Ring, p	D_p (cm)	I_p/I_1	ν_p (MHz)[a]	C_p (pF)
#1	1	5.0	1	114.1	25.43
	2	2.5	-1.13	102.3	71.67
#2	1	5.0	1	111.2	26.79
	2	2.5	-1.13	105.5	67.39
	3	15.0	-0.09	90.5	9.29

[a] Larmor frequency = 127.77 MHz.

Table 1 - Multi-Ring Surface Coil Design Parameters - D_p – ring diametner, I_p/I_1 – current ratio, ν_p – ring frequency, C_p – capacitor value

Optimized through simulations, two multi-ring surface coils were designed. The first, was a two-ring coil (Table 1) designed for homogenous B_1 over the VOI described above. The two co-planar and co-axial rings consisted of a "main" ring 5 cm in diameter with a conductor radius of 2.2 mm and a smaller "B_1-shaping" ring 2.5 cm in diameter with a conductor radius of 1.6 mm with opposite current 1.13 times that of the main ring current. In an attempt to improve SNR, a second coil was designed consisting of three-rings, the first two identical to the two-ring surface coil and a third ring designed to reduce the total power deposited in the sample. The third ring was 15 cm in diameter with a conductor radius of 3.2 mm and opposite current of 0.09 relative to the "main" ring. The same 3.84 cm diameter matching ring was used for both multi-ring surface coils.

5.1 Signal-to-Noise Ratio

SNR relative to a standard 5cm single-ring surface coil were measured and are shown in table 5.2

	Contamination	WS	SNR	
			Theoretical	Measured
Standard Surface Coil	1.0	1.0	1	1
Two-Ring Surface Coil	0.7	2.0	0.73	0.75
Three-Ring Surface Coil	----	----	0.83	0.85
CP Head Coil	----	4.0	----	0.3

Table 5.2. Comparison of SNR between standard RF coil and multi-ring coil.

Initially, intrinsic SNR values (column 4 of Table 5.3) were calculated to find the optimal multi-ring surface coil design. The first design (two-ring surface coil) provided localization characteristics similar to a volume coil and much improved over the standard surface coil. The experimentally determined SNR (column 6 of Table 5.2) for the two-ring surface coil was found to be 75% of that of the single-ring surface coil, a factor of 2.5 improvement in SNR over a circularly polarized head coil. The experimental SNR is in excellent agreement with the predicted SNR (column 5 of Table 5.2).

The three-ring coil provided an improvement of 13% over the two-ring surface coil with the same localization quality.

Although this design has focused on producing a more homogeneous B_1 field within a specified VOI, and therefore have tolerated losses in sensitivity, a multi-ring surface coil could also be designed specifically for sample noise reduction and consequently improved SNR. This might be achieved with a two-ring surface coil consisting of a "main" ring and a "noise-reduction" ring, similar to the third ring of our three-ring surface coil. SNR calculations show that up to 10% improvement in SNR over a standard surface coil could be expected.

As with standard surface coils, the SNR advantage of the multi-ring surface coil compared to a volume coil diminishes as the sample volume is made smaller and/or the VOI moved further from the surface, closer to the center of the volume (27, 28).

5.2 B1 Homogeneity

The axial 1-D B_1 field plots (Fig. 5 5.1) clearly show the improved B_1 homogeneity within the VOI for the two-ring surface coil over a standard 5-cm single loop surface coil. A comparison of the calculated axial B_1 field and the B_1 measured on the bench under loaded conditions is shown. There is a good agreement between the calculations and the loaded (Fig. 5 5.1). The reduced B_1 magnitude at the voxel location with respect to the standard surface coil is a consequence of the negative current in the "B_1-shaping" ring, and causes a loss in sensitivity of the multi-ring surface coil. For a quantitative measure of the B_1 homogeneity, the flip angle along the coil axis within the 1.0 cm voxel was calculated from the simulated 1-D field. For the standard surface coil, the maximum and minimum flip angles were 121° and 67° respectively (or 90° ± 27°) whereas for the multi-ring coil the maximum and minimum flip angles were 95° and 85° respectively (or 90° ± 5°).

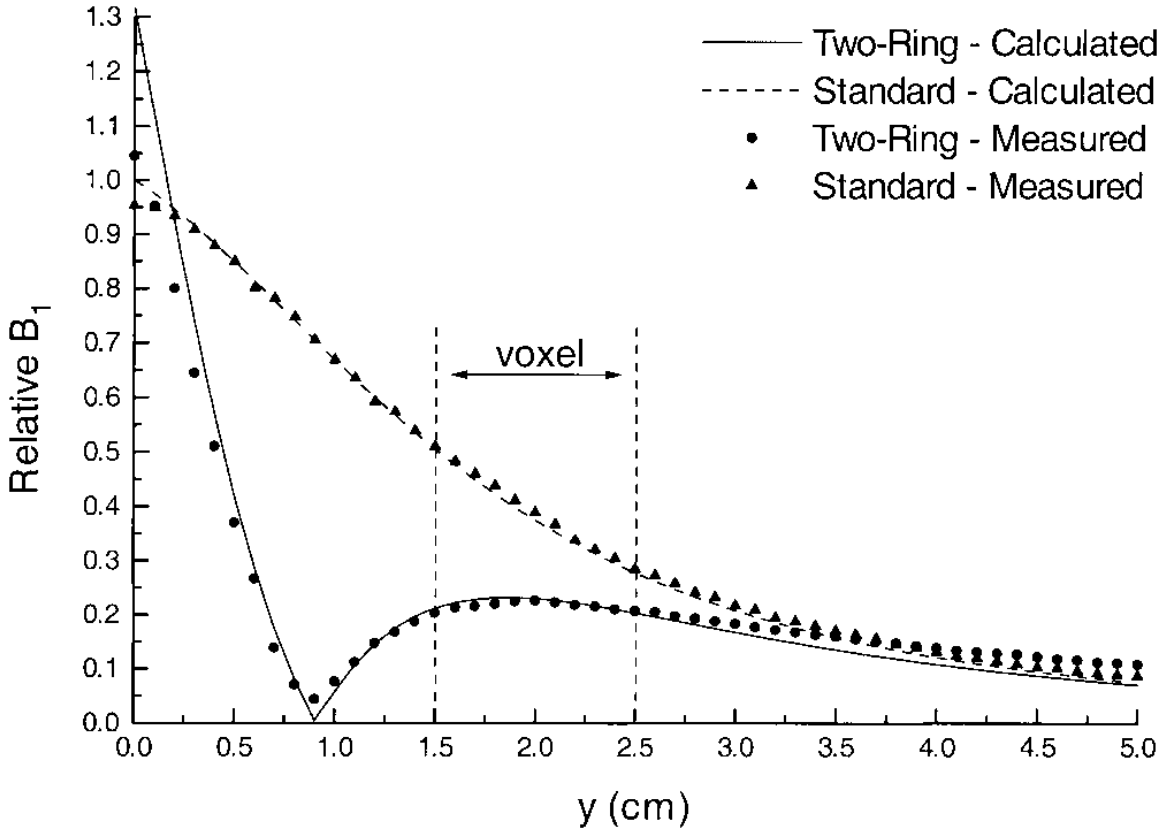

FIG. 5.1. Calculated and bench measurement of the B_1 field magnitude along the surface coil axis for the two-ring surface coil and the traditional surface coil. The size and position of the voxel of interest is shown.

Two-dimensional calculated B_1 field distributions in the y-z plane are shown in Fig. 5.2 and 5.3. Not only is there a more homogeneous B_1 within the voxel of intrest (VOI), but also a nulling of field about 1 cm from the sample surface. This effect could result in lowered contamination from signal outside the VOI as well as lowered noise pick-up when compared to standard surface coils.

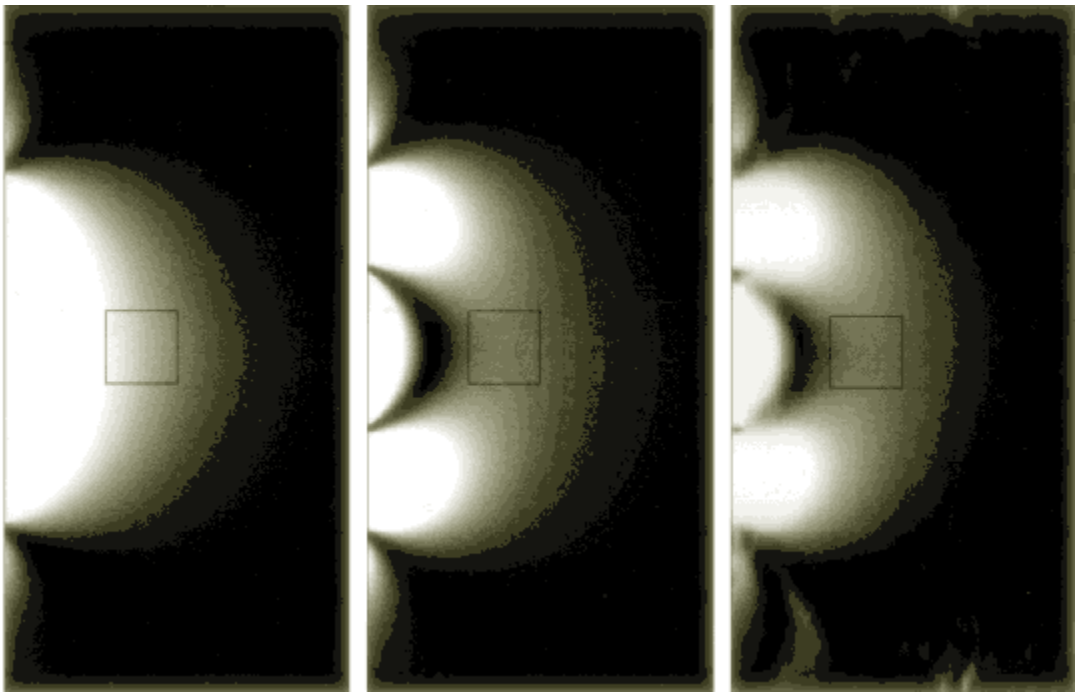

FIG. 5.2 – Calculated 2-D B_1 field distribution (y-z plane) for (a) the traditional surface coil and (b) the two-ring surface coil. (c) Experimental B_1 field map for the two-ring surface oil. Images are scaled to show the B_1 homogeneity within the VOI indicated.

The excellent localization quality (Fig. 5.3) of the multi-ring coil is demonstrated by images of the selected VOI and by signal profiles through the VOI. Simulations show that the two-ring surface coil produced a symmetric and homogenous response similar to a volume coil whereas the standard surface coil has the characteristic asymmetric axial profile. For comparison, simulated voxel profiles are also shown, where the standard surface coil is used as receive-only, with uniform excitation (volume coil or adiabatic pulses). The asymmetric voxel profile still occurs and again could result in inaccurate quantitation of average metabolite concentration from heterogeneous tissue.

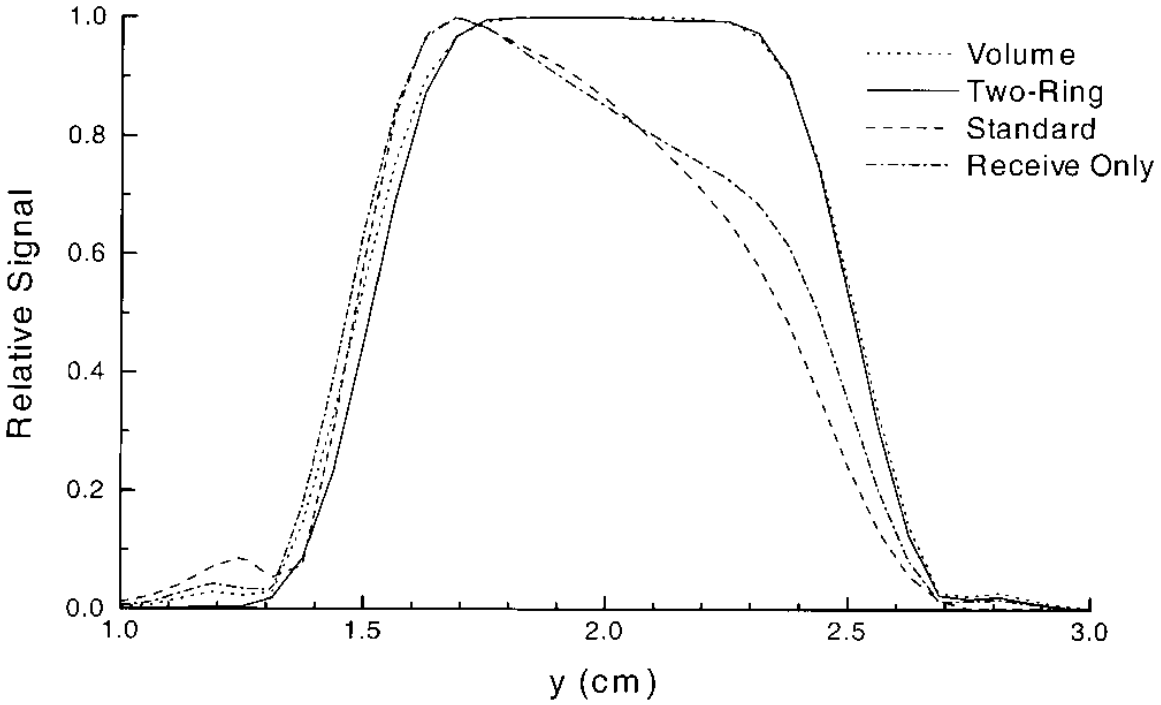

FIG 5.3 - Simulated voxel profiles for a volume coil (dotted line), the two-ring surface coil (solid line), the standard surface coil (dashed line), and the standard surface coil used as receive-only (uniform excitation) (dash-dot line). The 90° flip for the two-ring surface coil was at y ≈ 1.7cm from the sample surface.

Experimental STEAM voxel images in the y-z plane obtained with both the two-ring and standard surface coils and a CP head coil are shown in Fig. 8 5.4. The two-ring surface coil produced a homogenous VOI image similar to that of the head coil, whereas the standard surface coil has the characteristic asymmetric response. Experimental voxel profiles along the y-axis, shown in Fig. 5.4, clearly illustrate the similarity of localization with the two-ring surface coil and the head coil. The axial profile again demonstrates the improvement over the standard surface coil. There is very good agreement between the simulated and experimental axial voxel profiles.

FIG. 5.5 Experimental voxel images obtained with STEAM using (a) a circularly polarized head coil, (b) the two-ring surface coil and (c) the standard surface coil. Surface coils are located to the left of the corresponding image. FOV shown is 2 cm.

5.3 Specific Absorption Rate

One of the advantages surface coils have over volume coils is lower RF power requirements. This is particularly important for high-field MRIwhen large volume coils produce SAR that exceeds allowed by FDA limits. Table 5.3 compares the RF power required for spectroscopy and voxel imaging experiments (P_i), for the CP head coil (90° flip at y = 2.0 cm), standard surface coil (90° flip at y = 2.0 cm) and the multi-ring surface coils (90° flip at y = 1.7 cm). The quadrature volume coil required 11.1 dB (or 12.9 times) more power than the standard surface coil while the two-ring coil only required 4.5 dB (or 2.8 times) more. The additional power needed for these multi-ring surface coil designs can be attributed to decreased $\hat{B}_1$ with respect to the standard surface coil.

Calculated local SAR distributions for the standard and two-ring surface coil are shown in Table 5.3, where peaks in local SAR correspond to the conductor positions of the 5-cm rings. Results of the local and total SAR simulations are summarized in Table 5.3. As may have been expected from the additional power requirements, both the total

and peak local SAR values are higher for the two-ring surface coil than for a standard surface coil of similar dimensions. Although the total SAR is increased 2-fold, it is still much lower than typical volume coil total SAR limits.

	RF power (P_i)[a]	Total SAR[b]	Peak Local SAR
Standard Surface Coil	0 dB	1	1
Two-Ring Surface Coil	+4.5 dB	2.0	2.5
Three-Ring Surface Coil	+3.9 dB	----	----
CP Head Coil	+11.1 dB	----	----

Table 5.3 - RF power required as well as local and total SAR relative to a standard 5cm single-ring surface coil

[a]Input RF power used for spectroscopy experiments, referenced to the power delivered to the standard surface coil.

[b]Total SAR values are found from the input RF power and scaled with the *Q*-value**s**.

6. MULTI NUCLEAR RF COILS

The combination of MR imaging with spectroscopy provides a powerful tool for clinical management of problems such as stroke, tumor monitoring and the assessment of other diseases. Especially the integrated acquisition of proton images and localized spectra is essential for the practical application of spectroscopic techniques to human and animal research and it is highly desirably to use a singe RF probe in order to minimize operational problems such as changing coils from one experiment to another. Advantages of a such a probe in the form of a double-tuned coil also include more accurate localization of spectra and easier shimming for ^{31}P spectroscopy since the shimming can be done at the ^{1}H frequency with the same coil over the same volume. Absolute quantification methods using proton signal are as well easier to perform when correction for substantially different B_1 profile is not required.

Quantification of the tissue metabolites by heteronuclear MRS can be achieved using dual-frequency RF coils. The dual-frequency coils allow simultaneous measurement of two nuclei, without disruptions associated with exchanging coils for imaging and spectroscopy examinations. One of them is usually ^{1}H while other one is phosphorus (^{31}P) or sodium (^{23}Na). The proton frequency is used often for high-resolution imaging that allows lesion localization while other frequency is used for spectroscopic lesion analysis. Proton frequency provides the sensitivity needed for shimming. Dual-frequency coils should deliver SNR of the single frequency RF coil as well as produce homogenous RF field over the sample volume. To address these needs the double-tuned quadrature birdcage coils were developed. An example is a design based on two coaxial birdcage coils resonating at ^{31}P and ^{1}H frequencies. Such a coil

provides excellent ^{31}P performance although lower SNR for ^{1}H when compared to a single frequency ^{1}H coil. This design allows altering the ^{31}P coil length thus providing better SNR sacrificing however B_1 homogeneity (29). Another solution is to use the same size coils and tune every other leg of the coil to the desired frequency and use trap circuits and inductive matching to optimize the coil (30, 31).

Other solution uses surface coil with frequency splitting circuitry (32). This construction allows concurrent ^{1}H and ^{31}P MRS and provides the same B_1 homogeneity for both frequencies almost without reducing SNR when compared to the single frequency RF coils. The author of the thesis introduced a new generation of the RF coils for spectroscopy and imaging using the combination of multi-ring coil concept (32) with a multi frequency trap circuit (Fig. 6.1). This coil provides better SNR than a volume coil within the specified VOI, about 70% of the SNR of the single frequency surface coil, but it creates homogenous and identical B_1 fields for both frequencies over the desired VOI (Fig.6.2). The coil was patented by the author (34).

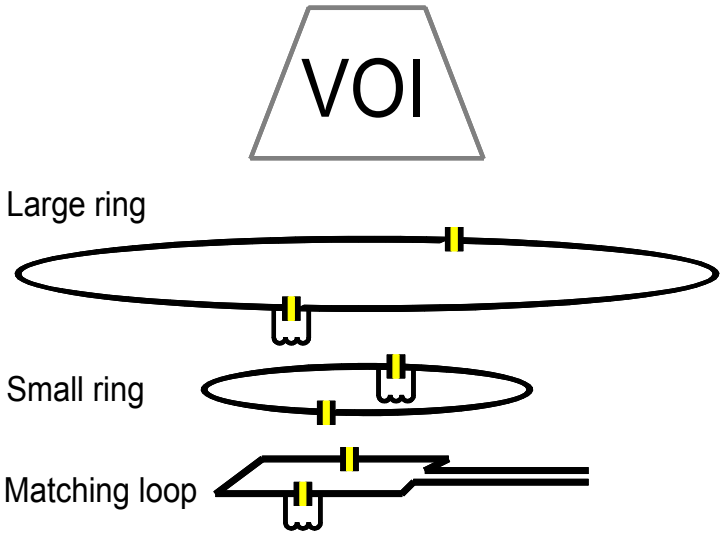

FIG. 6.1. Inductively coupled dual frequency RF coil.

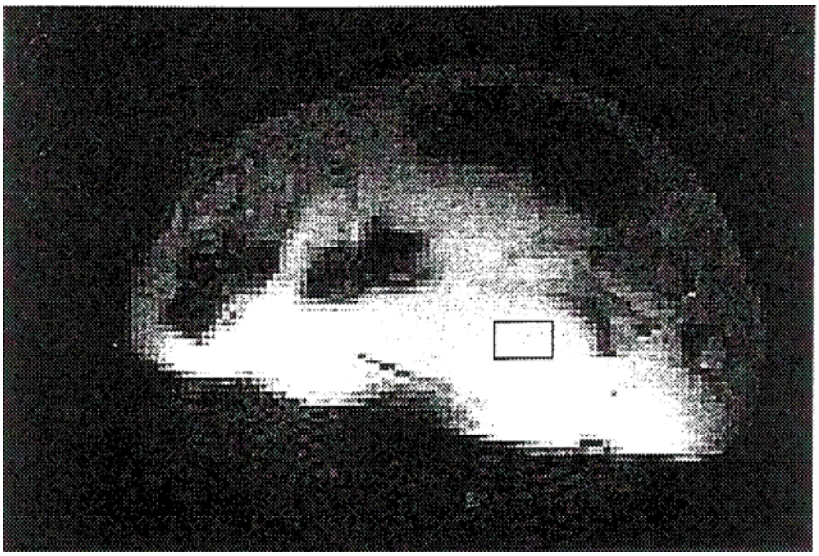

FIG. 6.2. Snapshot-flash proton image of a rat liver obtained with the dual surface coil of Fig. 6.1.

The probe provides excellent proton images and ^{31}P spectra from an image selected voxel in rat liver at 7T (Fig 6.3). The probe uses a double ring construction where each ring is tuned to a parallel LC trap to two or more different frequencies (Fig

6.1) A calculation of the values of the inductance and capacitance provided by the author allows the double coil arrangement to be tuned to the required frequencies with a peak of the homogeneity at each frequency occurring at the same distance from the coil and with good Q. The probe is powered by a driver coil adjacent to the probe by mutual inductance.

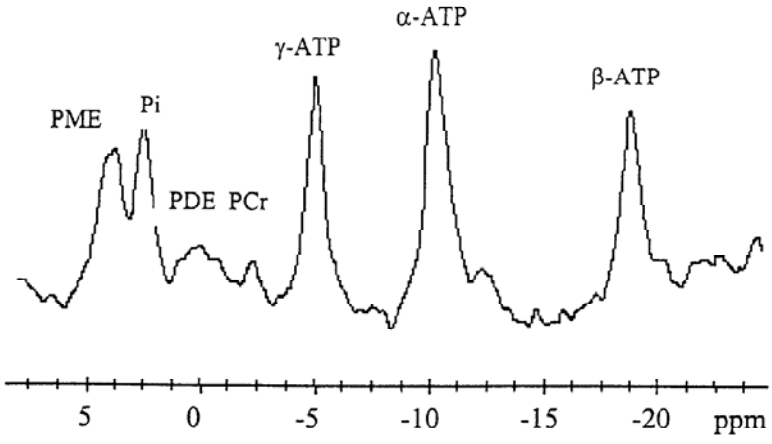

FIG. 6.3. Phosphorus spectrum from a voxel of the same liver.

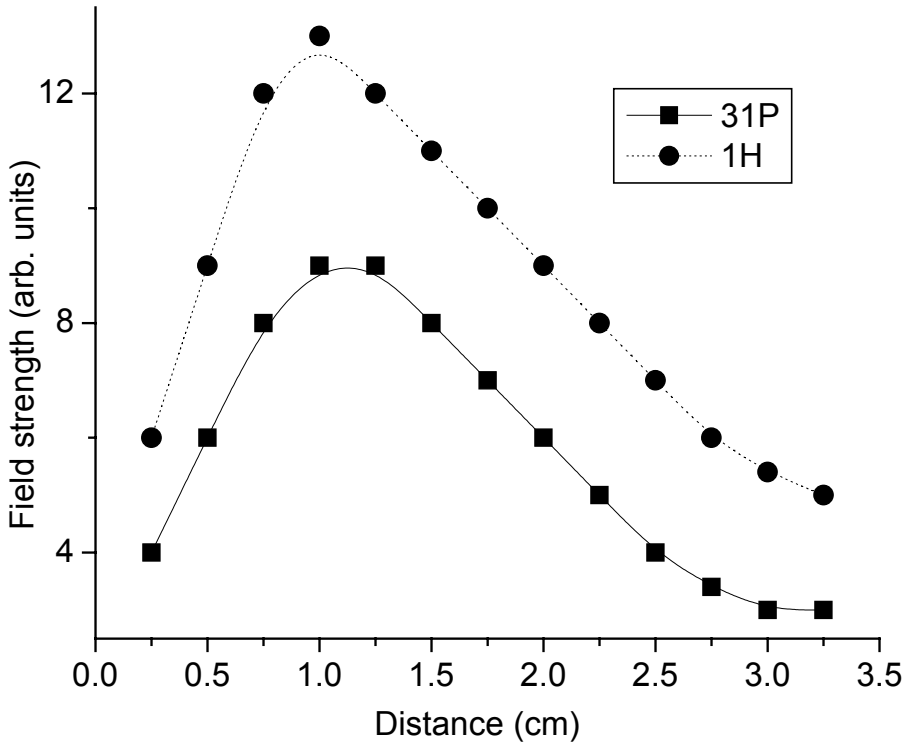

FIG. 6.4. Graph plotting the B_1 field (arbitrary units) produced by the two-coil assembly at different frequencies.

The coil was designed for imaging on the ^{1}H nucleus while spectroscopy was performed with the ^{31}P nucleus. However other frequencies can be selected for analysis of different nuclei.

The described coil was used for MRI and MRS on a rat liver, that is 10 to 15 mm deep inside the rat abdomen. To achieve a homogeneous B_1 field of proper frequency at a given VOI resonant frequencies and currents in individual rings were calculated using the Biot-Savart law. It was found that the following parameters provide the best B_1 homogeneity within VOI: diameters of small and large coils are 15 and 40 mm respectively with current ratio –1.4:1 for both ^{31}P and ^{1}H, and distance between coils of 4mm. To make the assembly resonate at 121.5 MHz and 300 MHz, the resonance

frequencies of the small ring were calculated, using the calculations described in Chapter 4, to be 113.7 MHz and 291.3 MHz. The large ring then has to resonate at 118 MHz and 296.3 MHz. Coupling between the rings and the double-resonant matching loop is achieved by a mutual inductance. Since the assembly in one example is constructed for a narrow bore magnet, a rectangular (40 mm x 50 mm) loop sliding along the bore is used for convenient matching.

Plots of the axial B_1 fields produced by a loaded dual-coil assembly at two frequencies of interest is shown in Fig. 6.4. The field strength is measured and presented in arbitrary units. It can be seen that the regions of B_1 homogeneity for both frequencies overlap and correlate with the theoretical calculations, used to optimize VOI.

Briefly, to obtain the desired current ratio, the inductance and reactance of both rings must be calculated to find the appropriate resonance frequencies of each ring. The mutual inductance between the rings, calculated from the coil geometry (ring radii and distance between them), then causes the two ring set to resonate exactly at the Larmor frequency. To make the coil resonate at two frequencies a splitting network reactance can be included.

Based on the Lenz's law, the reactance of the first and second ring is

$$x_1 = \frac{v_1}{l_1} = -j\omega_0 M_{12}\frac{l_2}{l_1} \qquad [6.1]$$

$$x_2 = \frac{v_1}{l_2} = -j\omega_0 M_{12}\frac{l_1}{l_2}. \qquad [6.2]$$

On the other hand the reactance of a ring with inductance L_p, capacitance C_p and frequency splitting network with a choke L_{spl} and capacitance C_{spl} is given by

$$x_p = x_{Lp} + x_{Cp} + x_{spl} = j\omega_0 L_p + \frac{1}{j\omega_0 C_p} + \frac{j\omega_o L_{spl} \dfrac{1}{j\omega_o C_{spl}}}{j\omega_o L_{spl} + \dfrac{1}{j\omega_o C_{spl}}}. \qquad [6.3]$$

The resonance frequency of each ring is then found by solving the equation

$$x_{Lp} + x_{Cp} + x_{spl} = 0. \qquad [6.4]$$

After tuning each ring to the appropriate frequency the rings are brought together to form the multi-ring surface coil. The two rings couple to create four resonant modes, with the second and the fourth modes producing the desired B_1 profiles at the Larmor frequencies ω_0 (e.g. 121.5 MHz and 300 MHz for ^{31}P and ^{1}H at 7T).

The experiment showed that the SNR for ^{1}H (300 MHz) of the doubly tunable double ring surface coil was identical to that of the double ring single frequency coil. At the ^{31}P resonant frequency (121.5 MHz) the SNR for the doubly tunable coil was about 72% of that of the single tuned coil.

The doubly tunable double ring surface coil was tested in MRI and MRS studies of rat liver in vivo at 7 T 21-cm horizontal bore magnet. FLASH proton image was acquired in the axial plane with TR/TE=3.7/2.2 ms, 2 mm slice thickness, 8x8 cm^2 field of view (FOV) and a matrix size of 128x128. A phosphorus spectrum was selected from a 2-s CSI experiment acquired with FOV 8.85 cm (horizontal) x 8.0 cm (vertical), TR=1 s, matrix size 8x8 zero-filled to 16x16, acquisition size 1k zero-filled to 4k, sweep width 4000 Hz, and processed with exponential line-broadening of 12 Hz and manual phase correction. Localized shimming on the liver was performed using a proton VOSY sequence with a 15x15x25 mm^3 (lateral, vertical and axial dimensions respectively) voxel with TE=20 ms, TM=30 ms. As can be seen from the spectrum, virtually no PCr contamination from abdominal muscle is observed.

7. BREAST RF COIL

Breast cancer is one of the most common malignancies in females. To reduce mortality, early detection and treatment are needed. MRI has proven to be valuable in the detection of breast tumors (35, 36) since it can provide 3D images of soft tissue not only of the breast but also of the axillary tail (37, 38). However, the highest resolution is needed for the detection of small tumors (39), and the RF probe design is a major factor in determining image quality and field of view (FOV). Initially, whole-body RF coils were used to image the human breast (40). However, smaller surface coils, which provide better signal-to-noise (S/N) ratio, were soon applied (41, 42) and various designs may be found in the literature: cylindrical coils (43), single (44) or two-turn solenoidal coils (45), multiturn, shaped coils (46), and coils with two chambers for imaging both breasts simultaneously (47). As in radiographic mammography, breast compression (48, 49) is often used, though mostly to reduce breast motion.

The optimal breast coil design should yield excellent S/N ratio and good $B1$ field homogeneity, yet allow imaging of both the breast and the chest wall as well as the axillary region, for tumors may occur in all these areas. Unfortunately, these requirements tend to be conflicting. To deal with these issues the author proposed a new design based on inductively coupled Helmholt-Peir probe. In addition shielding of the chest wall away from the breast, to reduce RF losses in the chest, was used and a substantial improvement in performance obtained.

To provide the highest S/N, and hence high spatial resolution, the first probe to image a single breast in the center of the 3T magnet. It comprises three separate, individually tuned, unconnected rings of conductor: a main Helmholtz pair, of radius and

nominal separation 6.8 cm, and a smaller coupling ring of radius 5.5 cm, arranged as shown in Fig. 7.1. The three coils are coupled by mutual inductance and the coupling ring is attached to a 50 V cable with a sleeve-type balun. Annular aluminum foil shields 20 mm thick were placed symmetrically above and below the probe, as shown in Fig. 7.1, on the surface and within the wooden patient bed.

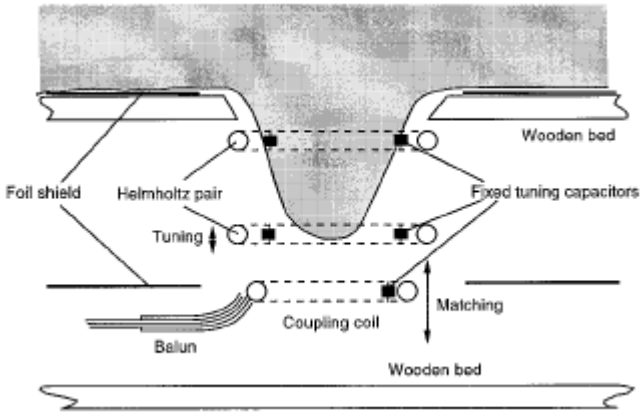

FIG. 7.1 - Breast coil components and shields. Two identical annular aluminum foil shields 15.5 cm ID and 45.7 cm OD are placed symmetrically above and below the probe.

FIG. 7.2 – The external view of the breast coil used for 1.5T GE system. One breast version of the coil, to keep the breast within the maximum field homogeneity, is presented.

To test the coil performance, single accumulation images at field strength 3 T were made with the gradient echo (GE), inversion-recovery GE (Fig. 7.2) and multislice spin-echo (SE) (Fig 7.3) techniques with various slice thicknesses, 256 x 256 matrix size and 14 x 14 cm FOV. A sagittal image with slice thickness 2 mm, matrix size 512 x 512, one accumulation and 14 x 14 cm FOV (Fig. 7.3), was also obtained. The resolution in this instance was 2 mm x 0.27 mm x 0.27 mm.

The images display excellent S/N in accord with the probe's superior Q-factor due to the judicious shielding. The measured image uniformity was consistent with the bench measurement of the $B1$ field (Fig. 7.4). In particular, a region up to 1.5 cm above the top shield was visible on most MR images for both SE and GE sequences. The chest wall is more visible in the GE than in the SE images due to the smaller sensitivity of the GE method to RF inhomogeneity. The SE sequence, however, could, if desired, be optimized for viewing the chest wall by the application of higher RF power. No image artifacts due to gradient-induced eddy currents in the foil shields were seen. This coil, when designed provided the best performance in comparison to any other RF coil.

FIG. 7.2. A sagittal IR gradient echo breast image (FA = 20°, TI = 900 ms, TR = 45.4 ms, TE = 7.4 ms, slice thickness 4 mm, matrix size 256 x 256, FOV = 14 x 14 cm).

FIG. 7.3. Sagittal spin-echo breast image (TR = 1200 ms, TE = 25 ms, slice thickness 2 mm, matrix size 512 x 512, FOV = 14 x 14 cm).

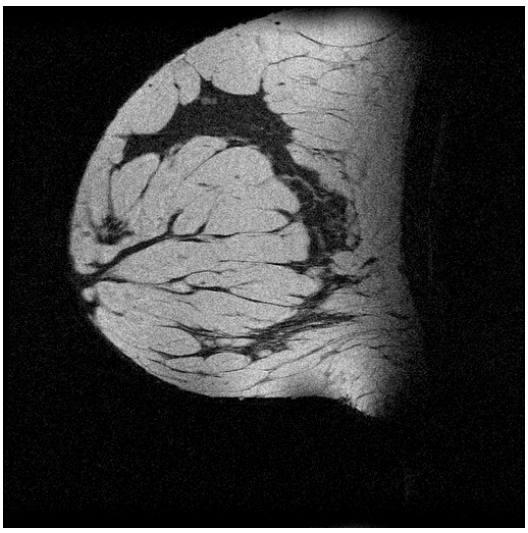

FIG. 7.4. Sagittal breast image with the resolution 500 μm × 320 μm × 320 μm.

The results demonstrate that it is possible, with the aid of RF shields, and using inductive coupling to view the chest wall adjacent to the breast while minimizing losses due to conductive tissue. Hence, breast images with good S/N ratio (~30), a slice thickness less than 2 mm, and in-plane resolution better than 0.3 x 0.3 mm can be readily obtained. Such resolution potentially allows for the detection of very small breast lesions, the majority of which have not yet metastasized, thereby making MRI a candidate for 3D breast screening (39).

A tradeoff is available, between improved S/N ratio at the chest wall and lower S/N over the rest of the breast, by manipulation of the shield aperture. The coil for both breasts was also designed and presented in Fig. 7.5.

FIG. 7.5. 1.5T breast rf coil (with the external cover).

8. HEAD RF COIL FOR INTRAPERATIVE MRI

MR technology has recently been introduced into neurosurgery bringing many advantages, such as accurate surgery planning, increased precision of the craniotomy and tumor resection, and decreased potential for complications such as hemorrhage or ischemia (50, 51).

In general there are four methods of intraoperative MRI: 1) surgery in the magnetic field, using open bore configuration MR scanners with a "double doughnut" design (51, 52), which allows access to the patient at the isocentre of the imaging system; 2) MRI that requires transportation of the patient (53, 54) to the imaging system; 3) MRI with a movable 1.5T magnet (55); 4) low-field MRI, typically from 0.064T to 0.3T using a permanent or resistive magnet (6, 8). Each of these concepts has its advantages and disadvantages, but each requires the maximum image resolution and minimal, if any, interference of the MRI system with a patient and operating field. Therefore an important element of the intraoperative MRI setup is the design of the operating table, radio-frequency (RF) probe and skull clamp, where both the operating table and the skull clamp must fulfill all standard requirements for operating room tools.

The probe and skull clamp design should also allow complete and unobstructed access for the surgical team to the patient's head without compromising sterility of the operating area. At the same time the RF probe must generate images of equal or better quality than standard RF probes. The design of the intraoperative RF probe should also permit the MRI system to be used as a standard radiological instrument without any modifications. The skull clamp should be suitable for a variety of performed surgical procedures and should also accommodate both adult and pediatric patients. It has to be

made of MRI-compatible materials and allow proper positioning of the RF probe for the imaging session. Both the RF probe and the skull clamp must form an integrated assembly suitable for patient imaging as well as any type of neurosurgical procedure. The entire assembly must also fit into the magnet bore.

The best performance is delivered by a volume, cylindrical coil [Fig. 8.1] but this coils is not suitable for intraoperative MRI. The intraoperative MRI systems reported to-date have used flexible transmit-receive surface coils (56) and different techniques of head immobilization. Such coils produce inhomogeneous images due to the decrease of the RF field with increasing distance between the coil and the region of interest; thus they are not suitable for high quality imaging of the entire brain. The MRI compatible Mayfield head frame has been used (57) in combination with the RF surface coils. The surgery was performed through the "holes" in the coils. A carbon-fiber frame and titanium stereotactic frame customized for the operating table also has been proposed (55). Freehand MR image guided procedure to monitor intracranial biopsy has been reported (58). Unfortunately none of the proposed designs meets all the requirements of the operating room environment.

Considering the limitations of the existing RF probes and skull clamps, an integrated RF head probe and skull clamp for the intraoperative MRI with a movable 1.5T magnet (55) were designed and manufactured.

FIG. 8.1 - Example of a standard RF quadrature birdcage for a human head (such a coil cannot accommodate skull clamp)

RF Probe

The inductively coupled rings were used as a base for the design of the coil for Intraoperative MRI. Computer simulations based on the Biot-Savart law showed, that the optimum B_1 field homogeneity is obtained with two rings in the same plane. However, such an arrangement did not provide enough space to accommodate the skull clamp. Therefore a computer program that included the skull clamp and table geometry was written to find a probe configuration that gave a good compromise between B_1 field homogeneity and access to the sensitive volume. This optimal design comprises four coaxial rings: one at 13 cm and a second at 17 cm above the center of the supine patient's head, with radii 17cm and 15 cm respectively, and two identical rings placed at the corresponding symmetrical positions below the head. Thus the head and a specially designed skull clamp can be accommodated. To ensure high quality (Q) value of the coil

and thus sensitivity, each ring is 23.3 mm in cross section. Currents in the outer and inner rings flow in the opposite direction with a current ratio -0.7. This probe produces a B_1 field with a homogeneity better than 95% within a 20 cm diameter spherical volume, but with the rapid fall-off outside that volume [Fig.8.2], providing self-shielding effect, and thus a high signal-to-noise (SNR) ratio. The major advantage of the design is that it may be separated into two parts: the lower two rings and the matching ring may be incorporated into an operating table, while the two upper rings, may be built into an easily sterilizable cover, which can be removed during neurosurgery [Fig.8.3]. Due to the inductive coupling there is no need for any electrical connection between the upper and lower parts. Sterility of the operating area during imaging sessions is ensured by sterile drapes placed over the operating field as well as the patient and securing the top part of the RF coil over the patient's head using posts supported by pins [Fig.8.3, 8.4, 8.5, and 8.6].

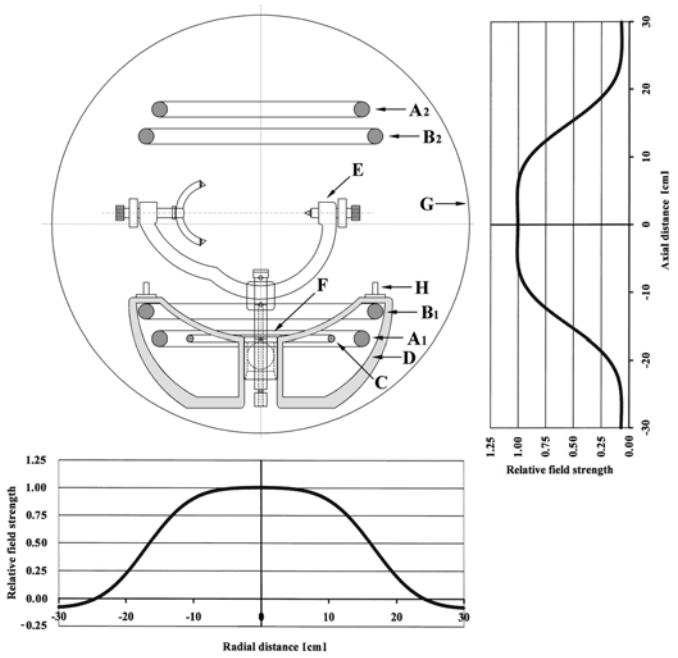

FIG. 8.2. Geometry of the integrated four-ring RF probe and skull clamp. $\mathbf{A_1}$ and $\mathbf{A_2}$: smaller, outer rings of 30 cm diameter. $\mathbf{B_1}$ and $\mathbf{B_2}$: larger, inner rings of 34 cm diameter. **C**: matching ring of 21 cm diameter. **D**: lower rings enclosure integrated within the operating table. The hydraulic system of matching and tuning is not shown. **E**: Asymmetric skull clamp with the ball joint **F**. **G**: RF shield. **H**: pins to position supporting posts of the upper enclosure. Radial and axial B_1 field profiles are also shown.

FIG. 8.3 Patient's head immobilized with the skull clamp inside the RF coil. Ready for imaging.

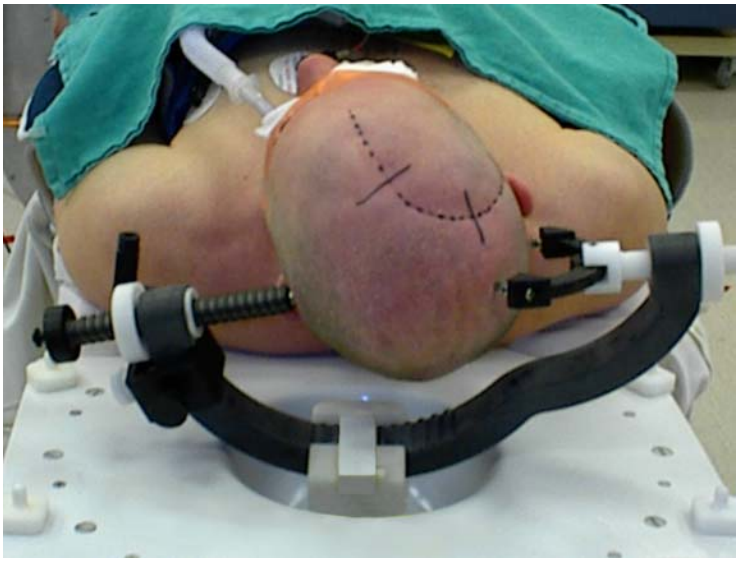

FIG. 8.4 Bottom part of the coil (imbedded in the table) and the skull clamp.

FIG. 8.5. The view of the Operating Room during the neurosurgery. Bottom part of the coil is hidden inside the patient table. The top part of the coil is away.

FIG. 8.6. Magnet moving over the patient during a neurosurgery

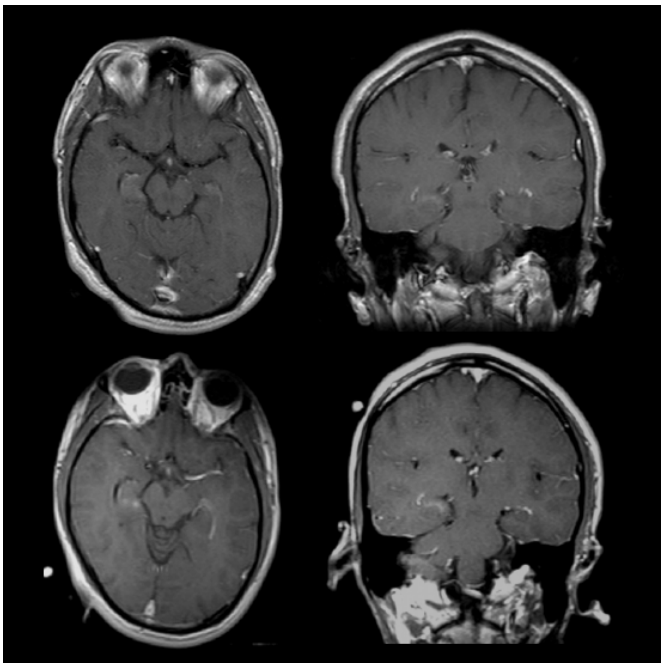

FIG. 8.7. Top row: diagnostic MR images obtained with a standard 1.5T scanner. Bottom row: surgical planning MR images obtained with the 4-ring integrated RF probe and skull clamp. Spin Echo imaging was used in both cases: TR=500ms, TE=13ms, matrix=256x256, slice thickness=5mm.

The method of coupled equations was used to determine reactances and resonant frequencies of the individual rings to ensure proper current ratio (25). Fine tuning in the range of ±250 kHz is accomplished by tilting the bottom large ring by ±2.5 mm, while the inductive matching adjustment is made by moving the fifth ring vertically. The matching ring is 21 cm in diameter with a 1.0 cm cross-section, tuned to exactly 63.78 MHz, corresponding to 1.5 T, and it is the only ring with electrical connections to transmit/receive tract. The remote tuning and matching adjustments are made with the aid of a non-magnetic hydraulic system.

A new technology for making the rings was also developed. Rings used for the coil were first cast with resin, covered with conductive copper paint, and then electroplated. A 1.0 cm gap in the copper layer was left for capacitors placed 90^0 apart on each ring.

An example of MR images obtained with the coil in the axial and transverse directions is shown in Figure 8.7(A). Figure 8.7(B) shows the MRI of the same subject obtained with a standard 1.5T system. As seen in Fig. 8.7 the image quality is comparable with both standard and 4-ring RF coil.

Skull Clamp

The three-point head fixation device has been widely used in neurosurgery. However, its standard version cannot be used for intraoperative MRI due to its incompatibility with MRI. Intraoperative MRI with a mobile 1.5T magnet sets additional specific requirements for the support equipment including a skull clamp that must fit to the head RF coil as well as to the magnet bore. The clamp cannot produce any MR artifacts due to its magnetic susceptibility or eddy currents created within, it cannot interfere electrically with the RF probe through mutual inductance or absorb RF energy which would cause tissue heating and image degradation. However it should give rigid skeletal fixation within the RF enclosure envelope while providing the surgeon with full freedom in positioning the fixation pins and the head. Therefore a new, dedicated skull clamp had to be designed and manufactured.

The specially designed skull clamp [Fig.8.8] comprises clamping arm assembly with the ball joint, both made of Delrin AF®, skull clamp frame (Tekamid™), rocker arm (Delrin AF®), and Mayfield® titanium skull pins to minimize eddy currents and susceptibility artifacts, yet ensuring the required holding strength. The frame was

asymmetrically shaped to fit to the probe enclosure as well as to accommodate the patient's head. The bottom ball joint allows for movement of the clamp in any direction. The arm can also be rotated independently to avoid critical areas of the skull while positioning the fixation pins. Infrared and MR reference markers can be attached to the clamp, allowing the infrared neuro-navigation system to be used.

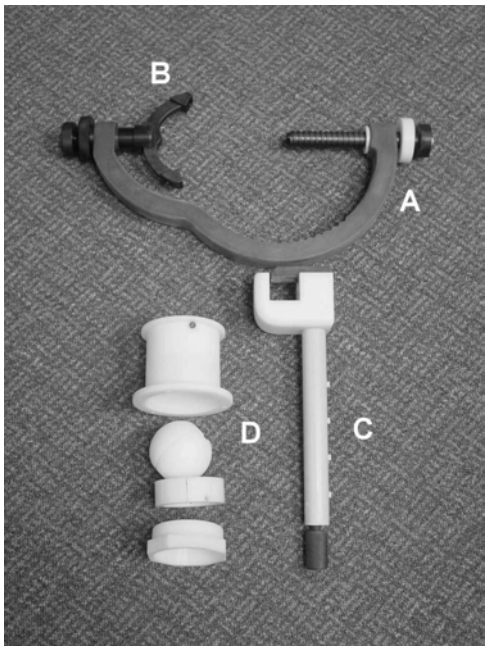

FIG. 8.8**.** Components of the skull clamp. A: skull clamp frame. B: rocker arm. C: clamping arm assembly. D: ball joint.

The described integrated RF probe and skull clamp has been successfully designed, constructed and used in the neurosurgical operating theatre as part of a 1.5T intraoperative system with movable magnet. The set-up employing our design can

provide all routinely acquired MR images of the 1.5T clinical MR system. Pre-, intra-, and post-surgical MR images have been obtained without compromising conventional surgical techniques. All positions could be accommodated with the coil. No MRI artifacts were observed in MR images. The assembly however is not restricted to the movable 1.5T system only. It could, with minor modifications, also be used with the other intraoperative systems described above.

Considering unobstructed access to the operating field, accommodation of any position provided by the 4-ring coil, the design of an integrated probe and skull clamp is a valuable component of the intraoperative MRI system. The RF probe and skull clamp is yet another step in the advancement of the intraoperative MRI towards the full integration of MRI technology with neurosurgery.

9. REFERENCES:

1. Abragam A. The Principles of Nuclear magnetism, Clarendon Press, Oxford, 1961. p.82.
2. Hoult DI, Richards RE. The signal-to-noise ratio of the nuclear magnetic resonance Experiment. J Mag Res 1976; **24:** 71-85.
3. Hoult DI, Lauterbur PC. The sensitivity of the zeugmatographic experiment involving human samples. J Mag Res 1979; **34:** 425-433.
4. Traficante DD. Impedance: what it is and why it must be matched. Concepts Magn Reson **1:** 73–92, 1989.
5. Traficante DD, Simms JA, Mulcay M. An approach to multinuclei capability in modern NMR spectrometers. J Magn Reson 1974; 1**5:** 484–497.
6. Chen CN, Hoult DI, Sank VJ. Quadrature detection coils—a further $\sqrt{2}$ improvement in sensitivity. J Magn Reson 1983; **54:** 324–327.
7. Hoult DI, Chen CN, Sank VJ. Quadrature detection in the laboratory frame. Magn Reson Med 1984; **1:** 339–353.
8. Hoult DI, Tomanek B. Use of mutually inductive coupling in probe design. Concepts Magn Reson Part B (Magn Reson Engineering) 2002; **15(4):** 262-285.
9. Lawry TJ, Kaczmar GS, Weiner MW, Matson GB. Computer simulation of MRS localization techniques: An analysis of ISIS. Magn Reson Med 1989; **9:** 299-314.
10. Matson GB, Meyerhoff DJ, Lawry TJ, Lare RS, Duijn J, Diecken RF, Weiner MW. Use of computer simulations for quantitation of ^{31}P ISIS MRS results. NMR Biomed 1993; **6:** 215-224.

11. Doornbos J, Grimbergen HAA, Booijen PE, Te Stroke L, Bloem JL, Vielovoye GJ, Boskamp E. Application of anatomically shaped surface coils in MRI at 0.5T. Magn Reson Med 1986; **3:** 270-281.

12. Axel L. Surface coil magnetic resonance imaging. J Comput Assist Tomogr 1984; **8:** 381-384.

13. McVeigh ER, Bronskill MJ, Henkelman RM. Phase and sensitivity of receiver coils in magnetic resonance imaging. Med Phys 1986; **13:** 806-814.

14. Lechter J. Computer-assisted design of surface coils used in magnetic resonance imaging: I. The calculation of the magnetic field. Magn Reson Imaging 1989; **7:** 581-583.

15. Moyher SE, Vingeron DB, Nelson SJ. Surface coil MR imaging of the human brain with an analytic reception profile correction. J Magn Reson Imaging 1995; **5(2):** 139-144.

16. Battocletti JH, Halbach RE, Sances A, Larson SJ, Larson RL, Bowman RL, Kudriavcev V. Flat crossed-coil detector for blood flow measurement using nuclear magnetic resonance. Med Biol Eng Comput 1979; 17: 183-191.

17. Bendall MR. Portable NMR sample localization method using inhomogeneous rf irradiation coils. Chem Phys Lett 1983; **99**: 310-315.

18. Styles P, Smith MB, Briggs RW, Radda GK. A concentric surface-coil probe for the production of homogeneous B_1 fields. J Magn Reson 1985; **62**; 397-405.

19. Reo NV, Ewy CS, Siegfried BA Ackerman JJH. High-field ^{13}C NMR spectroscopy of tissue *in Vivo*. A double-resonance surface-coil probe. J Magn Reson 1984; **58:** 76-84.

20. Den Hollander JA, Behar KL, Shulman RG. Use of double-tuned surface coils for the application of ^{13}C NMR to brain metabolism. J Magn Reson 1984; **57:** 311-313.

21. Roth K, Hubesch B, Meyerhof DJ, Naruse S, Gober JR, Lawry TJ, Bosko MD, Matson GB, Weiner MW. Non-invasive quantitation of phosphorus metabolites in human tissue by NMR spectroscopy. J Magn Reson 1989; **81:** 299-311.

22. Luyten PR, Groen JP, Vermeulen JWAH, den Hollander JA. Experimental approaches to image localized human ^{31}P NMR spectroscopy. Magn Reson Med 1989; **11:** 1-21.

23. Tomanek B, Ryner L, Hoult DI, Kozlowski P, Saunders JK. Dual surface coil with high-B_1 homogeneity for deep organ MR imaging. Magn Reson Imag 1997; **15:** 1199-1204.

24. Reitz JR, Milford FJ, Christy RW. Foundations of Electromagnetic Theory, 3rd ed. Massachusetts: Addison-Wesley; 1979. p. 242.

25. Hoult DI, Deslauriers R. A high-sensitivity, high-B_1 homogeneity probe for quantitation of metabolites. Magn Reson Med 1990; **16:** 411-417.

26. Giacolleto LJ. Electronic Designer's Handbook, 2nd ed. New York: McGraw-Hill; 1977.

27. Hayes CE, Axel L. Noise performance of surface coils for magnetic resonance imaging at 1.5 T. Med Phys 1985; **12:** 604-607.

28. Lawry TJ, Weiner MW, Matson GB. Computer modeling of surface coil sensitivity. Magn Reson Med 1990; **16:** 294-302.

29. Fitzsimmons JR, Beck BL, Brooker HR. Double resonant quadrature birdcage. Magn Reson Med 1993; **30:** 107.

30. Matson GB, Vermathen P, Hill TC. A practical double-tuned 1H/31P quadrature birdcage head coil optimized for 31P operation. Magn Reson Med 1999; **42:** 173-182.

31. Vaughan JT, Hetherington HP, Out JO, Pan JW, Pohost GM. High frequency volume coils for clinical NMR imaging and spectroscopy. Magn Reson Med 1994; 32: 206-218.

32. M.D. Schnall, H. Subramanian, J.S. Leigh, B. Chance, J. Mag. Res., 65, 122, (1985). Can not find (Tomanek, draft Radiofrequency Coils in Mag Reson Spec 47)

33. Volotovskyy V, Tomanek B, Corbin I, Buist R, Tuor UI, Peeling J. Doubly tunable double ring surface coil. Concepts in MR (Part B, MR Engineering) 2003, **17(B)1:** 11-16.

34. Tom;nek B, Volotovskyy V. Multiple Tunable Double Ring Surface Coil with High B_1 Homogeneity. US Patent 6,400,154 B2, June 4, 2002

35. Kaiser WA, Zeitler E. MR imaging of the breast: fast imaging sequences with and without Gd-DTPA. Radiology 1989; **170:** 681–686.

36. Kerslake RW, Carleton PJ, Fox JN, Imrie MJ, Cook AM, Read JR, Bowsley SJ, Buckley DL, Horsman A. Dynamic gradient-echo and fat-suppressed spin-echo contrast-enhanced MRI of the breast. Clin Radiol 1995; **50:** 440–454.

37. Pierce WB, Harms SE, Flamig DP, Griffey RH, Evans WP, Hagans JE. Three-dimensional gadolinium-enhanced MR imaging of the breast: pulse sequence with fat suppression and magnetization transfer contrast. Radiology 1991; **181:** 757–763.

38. Fossel ET, Brodsky G, DeLayre JL, Wilson RE. Nuclear magnetic resonance for the differentiation of benign and malignant breast tissues and axillary lymph nodes. Ann Surg 1983; **198:** 541–544.

39. Sivaramakrishna R, Gordon R. Detection of breast cancer at a smaller size can reduce the likelihood of metastatic spread: a quantitative analysis. Acad Radiol 1997; **4:** 8–12.

40. Ross RJ, Thompson JS, Kim K, Bailey RA. Nuclear magnetic resonance imaging and evaluation of human breast tissue: preliminary clinical trials. Radiology 1982; **143:** 195–205.

41. El Yousef SJ, Duchesneau RH, Alfidi RJ, Haaga JR, Bryan PJ, LiPuma JP. Magnetic resonance imaging of the breast. Radiology 1984; **150:** 761–766.

42. Stelling CB, Wang PC, Lieber A, Mattinghly SS, Griffen WO, Powell DE. Prototype coil for magnetic resonance imaging of the female breast. Radiology 1985; **154:** 457–462.

43. Ballon D, Morris EA, Schwartz LH, Giess C, Schneider E, Zakian KL, Koutcher JA. An asymmetric quadrature resonator for breast imaging at 1.5 tesla. In: Proceedings of the 5th Annual Meeting of ISMRM, Vancouver, Canada, 1997. p 1532. Tomanek Mag. Res. Med., 43: 917-920, 2000 9

44. Hornak JP, Szumowski J, Bryant RG. Elementary single turn solenoids used as the transmitter and receiver in magnetic resonance imaging. Magn Reson Imaging 1987; **5:** 233–237.

45. Merchant TE, Thelissen GRP, Kievit CE, Oosterwaal LJMP, Bakker CJG, Graaf PW. Breast disease evaluation with fat-suppressed magnetic resonance imaging. Magn Reson Imaging 1992; **10:** 335–340.

46. Sun L, Olsen JO, Robitaille PML. Design and optimalization of a breast coil for magnetic resonance imaging. Magn Reson Imaging 1993 ;**11**: 73–80.

47. Wolfman NT, Williams RW, Wall BE, Moran PR, Karstaedt N. Design modification of dedicated MR breast coil. J Comput Assist Tomogr 1986; **10:** 893–895.

48. Griswold MA, Hochman MG, Edelman RR. A compression plate breast array coil with reduced coil interactions. In: Proceedings of the 5th Annual Meeting of ISMRM, Vancouver, Canada, 1997. p 1530.

49. Heywang-Kobrunner SH, Huynh AT, Viehweg P, Hanke W, Requardt H, Paprosch I. Prototype breast coil for MR-guided needle localization. J Comput Assist Tomogr 1994; **18:** 876–881.

50. Alexander III E, Moriarty TM, Kikins R, Black P, Jolesz FM. The present and future role of intraoperative MRI in neurological procedures. Stereotact Funct Neurosurg 1997; **68:** 10-17.

51. Black PM, Moriarty T, Alexander E 3rd, Stieg P, Woodard EJ, Gleason PL, Martin CH, Kikinis R, Schwartz RB, Jolesz FA. Development and implementation of intra-operative magnetic resonance imaging and its neurological applications. Neurosurgery 1997; **41:** 831-842.

52. Hoult DI, Saunders JK, Sutherland G, Sharp J, Gervin M, Kolansky G, Kripiakevich D, Procca A, Sebastian R, Dombay A, Rayner D, Roberts F, Tomanek B. The engineering of an interventional MRI with a movable 1.5 Tesla magnet. J Magn Reson Imag 2001; **13:** 78-86.

53. Schenck JF, Jolesz FA, Roemer PB, Cline HE, Lorensen WE, Kikinis R, Silverman SG, Hardy CJ, Barber WD, Laskaris ET. Superconducting open-

configuration MR imaging system for image-guided therapy. Radiology 1995; **195:** 805-814.

54. Schulder M, Liang D, Carmel P. Cranial surgery navigation aided by a compact intraoperative magnetic resonance imager. J Neurosurg 2001; **94:** 936-945.

55. Martin AJ, Hall WA, Liu H, Pozza CH, Michel E, Casey SO, Maxwell RE, Truwit CL. Brain Tumor Resection: Intraoperative Monitoring with High-Field-Strength MR Imaging-Initial Results. Radiology 2000; **215:** 221-228.

56. Schwartz RB, Kacher DF, Pengolizzi RS, Jolesz FA. Intraoperative MR systems. Neuroimaging Clinics of North America 2001; **11(4):** 623-643.

57. Schwartz RB, Hsu L, Wong TZ, Kacher DF, Zamani AA, Black PM, Alexander III E, Stieg PE, Moriarty TM, Martin CA, Kikinis R, Jolesz FA. Intraoperative MR Imaging guidance for intracranial neurosurgery: Experience with the first 200 cases. Radiology 1999; **211:** 477-488.

58. Hall WA, Martin AJ, Liu H, Nussbaum ES, Maxwell RE, Truwit CL. Brain biopsy using high-field strength interventional magnetic resonance imaging. Neurosurgery 1999; **44:** 807-814.